Assessment of particle image velocimetry applied to high-speed organic vapor flows

Michelis, T.; Head, A. J.; Majer, M.; Colonna, P.; De Servi, C.

DOI
10.1007/s00348-024-03822-z

Publication date
2024

Document Version
Final published version

Published in
Experiments in Fluids

Experiments in Fluids (2024) 65:90
https://doi.org/10.1007/s00348-024-03822-z

RESEARCH ARTICLE

Assessment of particle image velocimetry applied to high-speed organic vapor flows

T. Michelis[1] · A. J. Head[2] · M. Majer[2] · P. Colonna[2] · C. De Servi[2,3]

Received: 15 November 2023 / Revised: 1 May 2024 / Accepted: 2 May 2024

Abstract

Compressible flows of fluids whose thermophysical properties are related by complex equations are quantitatively and can be qualitatively different from high-speed flows of ideal gases. Nonideal compressible fluid dynamics (NICFD) is concerned with these fluid flows, which are relevant in many processes and power and propulsion systems. Typically, NICFD effects occur if the fluid is an organic compound and its vapor state is close to the vapor–liquid critical point, at high-reduced temperature and pressure (even supercritical). Current design and analysis of devices operating in the nonideal compressible regime demand for validated simulation software, characterized in terms of uncertainty. Moreover, experiments are needed to further validate related theory. Experimental data are limited as generating and measuring these flows is challenging given their high pressure or temperature or both. In addition, flows of organic compounds can be flammable, can thermally decompose, and sealing may demand for special materials. Recently, more research has been devoted to the measurement of these flows using both intrusive and less intrusive techniques relying on optical access and lasers. The transparency and refractive properties of these dense vapors pose additional problems. The ORCHID (organic Rankine cycle hybrid integrated device) at the Aerospace Propulsion and Power Laboratory of Delft University of Technology is a closed-loop facility, used to generate a continuous nonideal supersonic flow of siloxane MM with the vapor at 4bar and 220 °C at the inlet of the test section. Within this work, we have employed particle image velocimetry for the first time to obtain the velocity field in a de Laval nozzle in such flows. Measured velocity fields (expanded uncertainty within 1.1% of the maximum velocity) have been compared with those resulting from a CFD simulation. The comparison between experimental and simulated data is satisfactory, with deviation ranging from 0.1 to 10 % from the throat to the outlet, respectively. This discrepancy is attributed to hardware limitations, which will be overcome in the future experiments. The feasibility of PIV with uncontrolled but fixed seeding density to measure high-speed vapors of organic vapors has been demonstrated, and future experimental campaigns will target flows for which nonideal effects are more pronounced, other paradigmatic configurations, and improvements to the measurement techniques.

1 Introduction

Compressible flows of dense vapors occur in several devices relevant to power and propulsion applications, such as valves, nozzles, diffusers, compressors, and turbines. The relation between thermodynamic properties of fluids in these flows departs significantly from that prescribed by the ideal gas law; therefore, simulating the motion of fluids in these thermodynamic states requires computation of their thermodynamic and transport properties by means of complex models. The branch of fluid mechanics dealing with this type of flows is called nonideal compressible fluid dynamics (NICFD). NICFD flows differ quantitatively and, in some cases, qualitatively from ideal gas flows Guardone et al. (2024).

✉ T. Michelis
t.michelis@tudelft.nl

1 Aerodynamics, Aerospace Engineering, Delft University of Technology, Kluyverweg 1, 2629HS Delft, The Netherlands

2 Propulsion and Power, Aerospace Engineering, Delft University of Technology, Kluyverweg 1, 2629HS Delft, The Netherlands

3 Energy Technology Unit, VITO, Boeretang 200, 2400 Mol, Belgium

Published online: 30 May 2024

Since the early 2000s, computational fluid dynamics (CFD) solvers originally developed for polytropic ideal gas flows have been extended in order to simulate flows of fluids in nonideal thermodynamic states. Solvers of the RANS equations were the first to be modified, while LES and DNS codes have been adapted only recently. However, the validation of such solvers against experimental data has been accomplished so far only to a limited extent Guardone et al. (2024). Major sources of uncertainty are the reliability of the adopted thermophysical models of the fluids, and of the turbulence models of RANS and LES solvers, whose closure parameters should be calibrated by means of experimental data.

The first validation of a RANS code for the simulation of nonideal compressible fluid dynamics (NICFD) flows accounting for both numerical and measurement uncertainties was performed by Gori et al. (2020). The authors compared simulation results obtained with the open-source software suite SU2 Economon et al. (2015) and Vitale et al. (2017) with pressure and Mach number measurements of the dense vapor flow of siloxane MDM expanding through a converging–diverging nozzle. The thermodynamic properties of the working fluid were estimated with a multi-parameter Span–Wagner equation of state (EoS) model. The comparison with experimental data demonstrated that the results of RANS simulations are sufficiently accurate for engineering applications. Analogous conclusions were reported by Fuentes-Monjas et al. (2023) for a validation case similar to that of Gori et al. (2020) but for a different working fluid, siloxane MM. CFD simulations were performed by computing fluid properties with a simpler thermodynamic model based on the cubic Peng–Robinson EoS embedded in SU2 Vitale et al. (2015).

A more encompassing and satisfactory validation of NICFD solvers has not been achieved yet as multiple accurate experimental datasets of paradigmatic compressible flows covering a representative range of conditions are not available. Measurements of NICFD flows are challenging as the fluid is either at high pressure or high temperature or both, and can be flammable. New dedicated facilities have been commissioned and started operation only recently (Spinelli et al. 2020; Guardone et al. 2024). Their common objective is to provide experimental data related to paradigmatic NICFD flows such as, e.g., adiabatic nozzle expansions (Spinelli et al. 2018; Robertson et al. 2020; Head et al. 2023), flows with shock waves (Zocca et al. 2019; Conti et al. 2022), and flows through blade cascades (Baumg ärtner, David, John J Otter, and Andrew PS Wheeler, 2020; Manfredi et al. 2023).

Optical flow measurement techniques, such as particle image velocimetry (PIV), are arguably suitable for providing accurate datasets for CFD validation purposes as it is possible to obtain velocity field data with high spatial and temporal resolution. Some initial attempts at using optical techniques to measure the velocity field of a flow of organic vapors are reported by Gallarini et al. (2016), who documented the design and commissioning of a particle seeding system suitable for LDV or PIV experiments, specifically conceived for operation with dense organic vapor flows, and by Head et al. (2019), who demonstrated the feasibility of the planar PIV technique to study flows of siloxane vapors. More recently, Valori et al. (2019) applied PIV to characterize the natural convection flow of an organic fluid in supercritical thermodynamic states. The PIV measurements documented in Head et al. (2019) and in Valori et al. (2019) are related to incompressible flows, though. To the authors' knowledge, the only experimental studies about direct velocity measurements in NICFD flows are those of Ueno et al. (2015) and of Gallarini et al. (2021). Ueno et al. (2015) obtained the velocity field of a two-phase CO_2 flow expanding through a nozzle by means of the PIV technique. Gallarini et al. (2021) demonstrated the implementation of the two-dimensional laser Doppler velocimetry (LDV) technique to measure the flow velocity of a siloxane vapor along the axis of a planar nozzle in both subsonic and supersonic conditions.

This article presents the first-ever application of the PIV technique to measure the velocity field of a flow of a dense organic vapor expanding through a de Laval nozzle to supersonic conditions, from a mildly nonideal thermodynamic state at moderate pressure and temperature. The nozzle test section is installed in the ORCHID (organic Rankine cycle hybrid integrated device), a research facility in the Aerospace Propulsion and Power Laboratory of Delft University of Technology. The ORCHID setup allows to perform both fundamental studies on NICFD flows and to test organic Rankine cycle (ORC) components (Head 2021). The ORCHID balance-of-plant is a state-of-the-art high-temperature recuperated ORC system and is capable of delivering vapor flows at temperatures and pressures of up to 350° C and 25bar at the inlet of the test sections. The setup has been designed taking into consideration the possibility of using many different working fluids. Siloxane MM (hexamethyldisiloxane) has been selected for the first experimental campaigns. The test section used in the experiment documented here includes a two-dimensional converging–diverging nozzle with optical access. The obtained flow velocities were successfully compared with those resulting from a CFD simulation.

2 Methodology

2.1 Experimental configuration

Figure 1 shows a schematic cross-section of the de Laval nozzle and installed in the ORCHID setup. The enclosure is made of 316Ti stainless steel. The PIV imaged field of view is also indicated. The nozzle profile is designed with the method of characteristics, see Head (2021) for more details. The working fluid is MM. The total conditions of the working fluid flow at the nozzle inlet are $T_\mathrm{t} = 220 \pm 0.64°$ C and $p_\mathrm{t} = 4 \pm 0.0302$bar, while the nozzle static back pressure is $p_\mathrm{s} = 0.2981$bar (see Fig. 2). These values are the average of the measurements recorded during the experiment by temperature and pressure probes installed upstream and downstream of the nozzle. Additionally, these quantities are used to define the boundary conditions of the flow simulations performed for comparison, see Sec. 2.3.

The origin of the Cartesian coordinate system used to define locations for both measured and computed quantities is in the geometrical throat of the nozzle. The nozzle total length and span at ambient conditions are 75 mm and 20 mm, respectively, and the nominal throat height is 7.5 mm. At the operating conditions of the experiments, the throat height changes due to the thermal expansion of the nozzle housing (of approximately 300-mm hydraulic diameter) and to the softening of the Viton™ gaskets at the interface between the nozzle profiles and the nozzle housing. This geometric change is optically tracked by locating the two cross indicators machined at $x = 0mm$ on the nozzle sides, as shown in Figs. 1 and 3a. Spatial calibration based on a polynomial fit model is performed using an optical target with the same shape as the nozzle (Fig. 3a), allowing for additional correction of geometrical lens distortions. Based on this spatial calibration, the throat center is defined as the midpoint between the cross indicators, whereas the throat height is the distance between the cross indicators minus their distance from the nozzle edge. The throat height estimated for the conditions of the experiment is 7.92 mm. The nozzle CAD model used to define the geometry of the flow for the CFD simulation is, therefore, based on this value of the throat height.

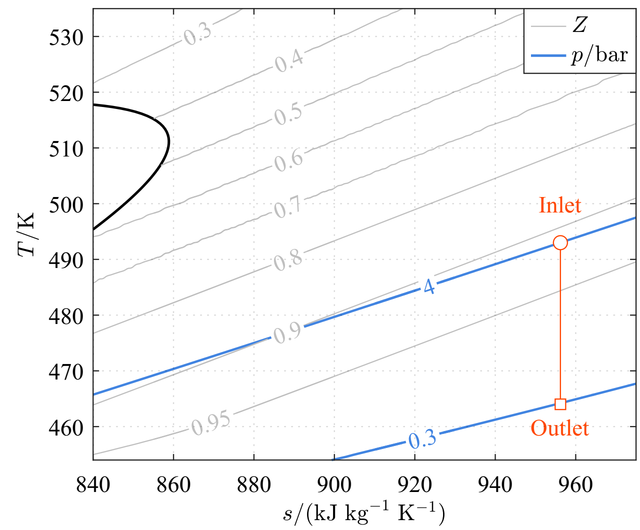

Fig. 2 T-s thermodynamic property diagram of siloxane MM, showing the saturation line, the vapor–liquid critical point, contours of the compressibility factor Z, and the isobars for the values of the total pressure at the nozzle inlet and static pressure at the nozzle outlet. The isentropic expansion occurring in the nozzle during the experiment ($p_\mathrm{t} = 4$bar, $T_\mathrm{t} = 220\ \circ C$, and $P_\mathrm{s} = 0.2981$ bara) is also indicated. Fluid properties are estimated with the in-house program FLUIDPROP implementing the Peng–Robinson cubic equation of state model with the Stryjek–Vera improved modification van der Stelt et al. (2012)

2.2 Velocity measurements

PIV is used to measure the two-component velocity field associated with the $x - y$ plane located at the midspan of the nozzle, i.e., at a 10-mm distance from the nozzle lateral walls. Spatial calibration is performed with the target and polynomial model mentioned in Sec. 2.1, achieving a resolution of approximately 29 px/mm. A summary of the PIV system specifications pertinent to the experiment is given in Table 1.

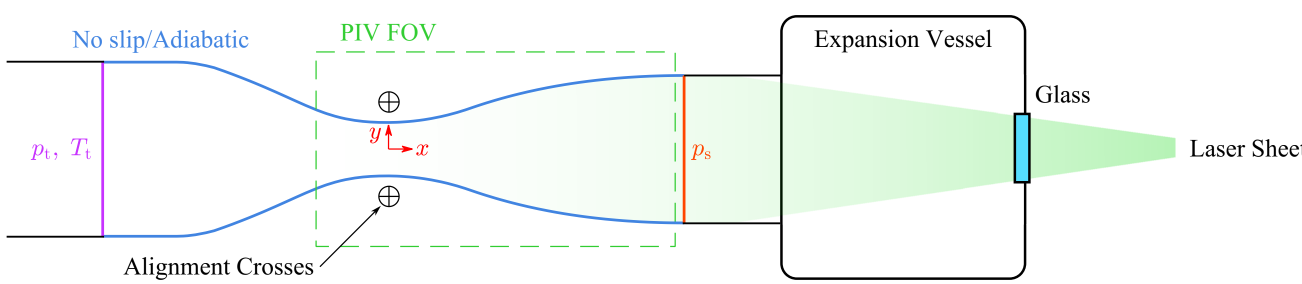

Fig. 1 Schematic of the nozzle test section (not to scale), indicating the PIV field of view (FOV). The computational domain for the flow simulations used for comparison to the experiment is indicated with blue lines corresponding to the nozzle walls and with purple (inlet) and red (outlet) lines for the boundaries normal to the flow direction. The scheme displays, in addition, alignment crosses used to estimate the throat height during the experiments, which varies depending on the fluid temperature. The origin of the Cartesian coordinates is set at the nozzle throat and used to define locations in both flow experiments and simulations

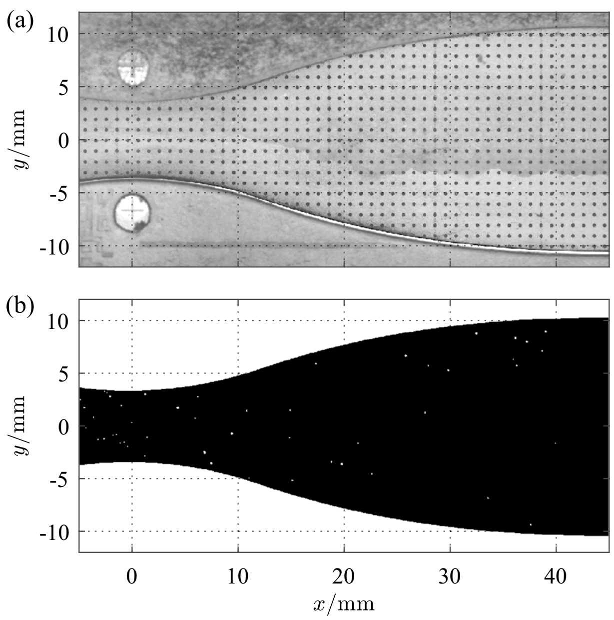

Fig. 3 **a** Image of the calibration target and throat alignment crosses. **b** Instantaneous PIV image depicting the typical observed particle concentration and size

Table 1 PIV system specifications

Parameter	Value
Sensor resolution	1628×1236
Pixel pitch	4.4μ m
Lens focal length	75 mm
Aperture ($f_{\#}$)	8
Frame separation (Δt)	5μ s
Magnification factor	0.13
Field of view area	56×27 mm^2
Vectors per field	102×55
Vector pitch	0.55 mm
Resolution	29 px/mm

Illumination is provided by a dual cavity Quantel Evergreen Nd:YAG laser, which delivers green light (532 nm) at 200 mJ per pulse. The beam is transformed to a sheet of approximately 1 mm thickness with a top-hat illumination profile, using a series of spherical and cylindrical lenses as well as two parallel knife edges. The region of interest is imaged with a LaVision Imager LX 2 MP camera and a 75-mm Tamron C-mount objective, set at an aperture of $f_{\#} = 8$. The camera sensor is cropped to obtain a field of view of 56×27 mm^2, and an ensemble of 5000 image pairs ($\Delta t = 5\mu s$) is recorded. Each recording realization contains on average about 50 particles in the field of view, the diffraction pattern of each forming a diameter of approximately 4 pixels on the camera sensor (see Fig. 3b).

For this preliminary study, a low particle seeding concentration was sought for in order to avoid the possibility of severe contamination of the facility. To this end, the small quantity of titanium dioxide particles (Ragni et al. 2011; Stöhr et al. 2012, TiO_2, typically used for the PIV seeding of supersonic and combustion flows, see, e.g., the works of) already present in the facility due to preliminary seeding tests was sufficient. The size of particles in the fluid suspension is assessed with the dynamic light scattering (DLS) technique, (see Stetefeld et al. 2016; International Standard 2017, for a comprehensive overview), using a stirred sample of the working fluid collected downstream of the nozzle after the experiment.

The sample preparation and procedure of determining the particle size is executed as follows: 1. A background/blank measurement is made with a control sample, MM in this case, to check for the presence of dust or particulates which might already be present. A pure and uncontaminated 2-ml sample is prepared in a 1-cm glass tube (centrifuge for 30 s). These external surface of these tubes are cleaned with ethanol to remove dust particles, fingerprints, and other contaminants. The tube is then placed into the DLS instrument chamber holder. After the instrument has finished the measurement, the count rate is then computed, which should be lower than the threshold of approx. 20 kHz. There will be no correlation in this case; 2. the sample taken downstream of the nozzle is the prepared in the same way as step 1. The DLS instrument reports reliable results when the input count rate is at least three times larger than the background value. The MM sample reported values of 110 kHz which is sufficient to compute the correlation curve. An exponential fit model with 250 grid points is used to determine the distribution function which allows to compute the mean peak position of the particle radius.

The results of three independent measurement runs of the sample are shown in Fig. 4. The measurement accuracy on particle size is ISO 13321/22412 compliant International Standard (2017) and thus within 2% of the stated size. The estimated diameter of the particles ranges approximately between 13 nm and 16 nm. This value is comparable to the median value provided by the particle manufacturer (Kemira P170, primary crystal size 14 nm, and bulk density 150 g/ł). No particle clustering was observed in either the DLS measurements nor the PIV images.

In order to assess the dynamic response of the 14-nm TiO_2 particles at hand, their relaxation time in siloxane MM was estimated in our past investigations to be approximately $\tau = 0.41\mu s$ Lakkad (2017). This value is comparable to the typical relaxation time reported in air and combustion flows ($< 5\mu s$), as observed in the works of Urban and Mungal (2001), Scarano and van Oudheusden (2003),

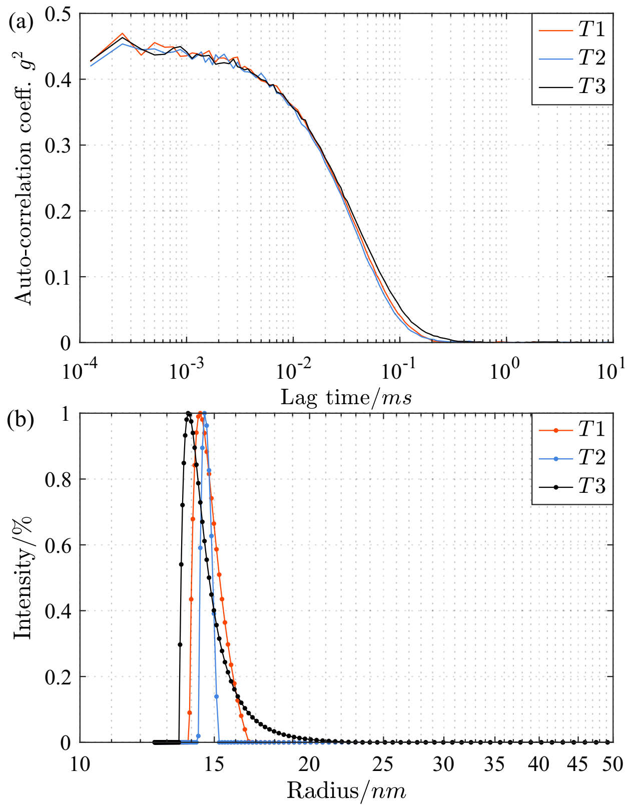

Fig. 4 Dynamic light scattering (DLS) measurements to determine the seeding particle size in samples of the working fluids, for three independent particle sizing tests ($T1$, $T2$, and $T3$). **a** Second-order auto-correlation coefficient of the DLS intensity trace and **b** measured particle size distribution

and Stöhr et al. (2012), for TiO_2 particle diameters below 50 nm. The maximum streamwise velocity observed in our current measurements is $u \approx 330m/s$. At the same time, since the flow is uniform (i.e., no relevant flow structures) and the aim is to compare velocities between simulations and experiments, a length scale equal to the throat height ($l = 7.92mm$) may be considered. This leads to an estimated particle slip velocity is $\Delta u = \frac{\tau u^2}{2l} \approx 2.8m/s$. Consequently, the expected velocity error due to particle slip ($\Delta u/u$) is within 1% along the streamwise direction. Similarly, for the maximum y–direction velocity component ($v \approx 83m/s$), the error due to slip is estimated to be below 2%.

An important consideration which may affect the optical measurements is the variation of the refractive properties of the flowing fluid and, therefore, the variation of the gradient of refractive index resulting from the variation of its density. To assess this effect, in line with the past studies Gallarini et al. (2021), the refraction index associated with each location within the field of view is calculated with the Gladstone–Dale equation,

$$n = 1 + k\rho, \tag{1}$$

where $k = 4.5 \times 10^{-4} m^3/kg$ is the Gladstone–Dale constant for MM, and ρ is its density, whose variation is estimated by means of the CFD simulation. The displacement deviation along the x and y directions is subsequently calculated as

$$\delta_x = \frac{L^2}{2}\frac{1}{n}\frac{\partial n}{\partial x},\ \ \delta_y = \frac{L^2}{2}\frac{1}{n}\frac{\partial n}{\partial y}, \tag{2}$$

where $L = 1$cm is half of the test section span. The estimated deviations are $\delta_x = 15\mu$m and $\delta_y = 8\mu$m, occurring in locations where the value of the refractive index gradient is high, i.e., in the vicinity of the nozzle throat. In regions where the flow is uniform, these deviations drop well below 1µm. Given the calibration resolution (29px/mm), deviations along the x and y directions correspond to 0.44 px and 0.23 px on the camera sensor. Since these values are within one camera pixel, deviations due to refractive index variation cannot be detected. Hence, it is concluded that, for the conditions of this experiment, uncertainties in the velocity field are only dependent on the PIV methodology.

Due to the particle concentration, particle displacement is calculated with a multi-pass, sum of cross-correlation algorithm (Scarano and Riethmuller 2000) using deforming non-overlapping interrogation windows Scarano (2001). The procedure is implemented in LaVision DaVis v. 10. The interrogation window size ranges from an initial 64 × 64 pixels to a final of 12 × 12 pixels. The resulting vector pitch is 0.55 mm in both x and y directions. Spurious vectors are identified and removed by setting a correlation threshold of 0.1 and by applying the universal outlier detection method Westerweel and Scarano (2005) to each interrogation window pass. The time-averaged uncertainty is estimated via linear error propagation Schiacchitano and Wieneke (2016) on the cross-correlation field. The estimated maximum expanded uncertainties on the time-averaged u and v due to PIV post-processing are $\varepsilon_{\overline{u}} \approx \pm 3.8m/s$ and $\varepsilon_{\overline{v}} \approx \pm 2.5m/s$, respectively (1.1% and 0.7% relative to the maximum velocity amplitude).

2.3 Flow simulation

A two-dimensional RANS simulation was performed in order to provide complementary velocity data, aiming to validate CFD codes and at the same time, assess the suitability of the PIV methodology. The adopted flow solver is the open-source code SU2 (Economon et al. 2015). The solver has been previously verified for the simulation of nonideal compressible flows by Pini et al. (2017) by comparing its results to those obtained with a state-of-the-art commercial solver. More recently, Head et al. (2023) and Fuentes-Monjas et al. (2023) verified the accuracy of the SU2 flow solver

Table 2 Main property values used as inputs of the CFD model

Parameter	Value
Inlet stagnation pressure ($P_{\mathrm{t,in}}$)	4bar
Inlet stagnation temperature ($T_{\mathrm{t,in}}$)	220.42° C
Outlet static pressure ($P_{\mathrm{s,out}}$)	0.298bar
Specific heat ratio (barγ)	1.0276
Thermal conductivity (barκ)	0.0255W /(m.K)
Dynamic viscosity (barμ)	$0.9957 \times 10^{-5} Pa.s$

by comparing simulation results with Mach values obtained from schlieren images and static pressures measured along the nozzle profile, for an expansion of MM similar to that considered in this work, though with higher total pressure and temperature values at the nozzle inlet.

The computational grid consists of a hybrid mesh made of 217k cells, sufficiently fine to guarantee grid independent results Head (2021). The structured boundary layer mesh at the nozzle wall ensures a $y^+ < 10$, which is commonly deemed as satisfactory in combination with the one-equation Spalart–Allmaras turbulence model. The Jameson–Schmidt–Turkel scheme (JST) was used as the advection scheme, which introduces second- and fourth-order numerical dissipation.

The thermodynamic properties of the fluid are calculated with the polytropic Peng–Robinson cubic equation of state model available within SU2. Hence, the caloric part of the isentropic process exponent was calculated as the average ratio of ideal gas specific heats at the inlet and outlet of the nozzle. The thermal conductivity and dynamic viscosity values are considered constant and are estimated using a well-known property estimation program Lemmon et al. (2018) as the average between the values at the inlet and at the outlet of the nozzle. The thermodynamic model is deemed appropriate for the considered operating conditions, as demonstrated by the numerical simulations reported by Bills (2020). The boundary conditions for the simulation are specified in terms of stagnation pressure and temperature at the inlet, and static pressure at the outlet (Table 2). The values of pressure and temperature are obtained by averaging the experimental pressure and temperature data.

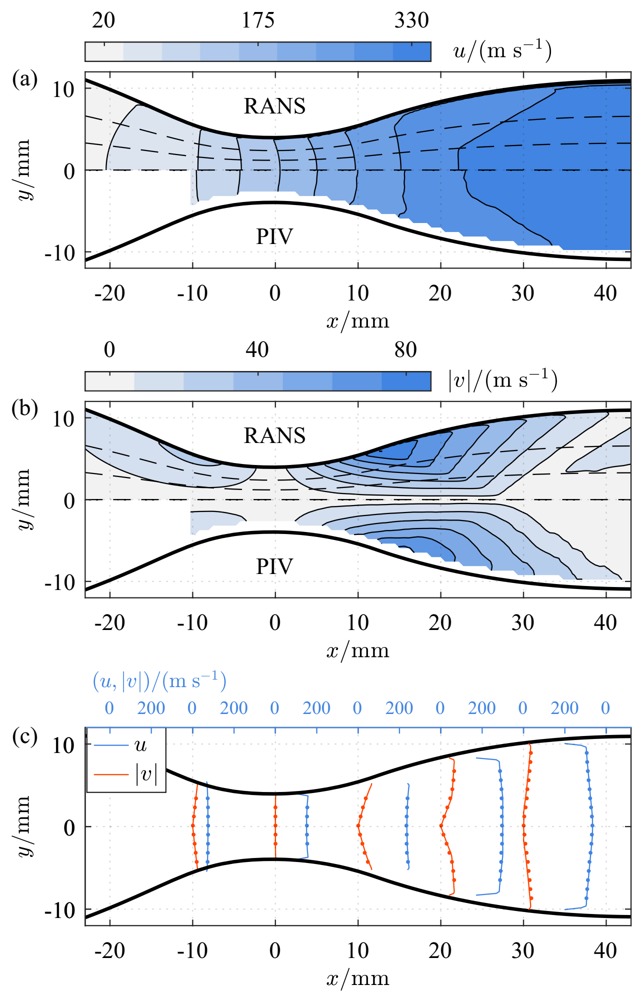

Fig. 5 Comparison between velocity component contours estimated by means of CFD simulation and PIV: **a** x-direction component, u and **b** y-direction component magnitude, $|v|$. The upper half of the flow domain reports values calculated with the RANS simulation, while the lower half reports values obtained with PIV. Dashed lines indicate the location where the velocity shown in Fig. 6 are extracted from. **c** u and $|v|$ profiles at various streamwise locations, with solid lines and points indicating RANS and PIV data, respectively. The experimental data have been reduced by a factor of two for clarity, while the magnitude of the u and $|v|$ velocity profiles correspond to those of the contours shown in (**a**) and (**b**), respectively

3 Results

3.1 Velocity field

Figure 5a and b shows the comparison between the measured u and v velocity component with homologous data obtained with a RANS simulation. As suggested by the symmetry of the velocity component fields about $y = 0$ shown in Fig. 5c, remarkable agreement between the experimental and numerical results is achieved. As expected, the magnitude of the streamwise component u significantly increases downstream of the nozzle throat due to the flow expansion. In turn, the value of the v component is higher where the nozzle cross-sectional area increases more steeply, while values are close to zero in the proximity of the throat as well as along the nozzle mid-plane ($y = 0$). Although RANS simulations provide results also for the boundary layer, PIV near the wall is unfeasible due to limitations of the current experimental setup; therefore, boundary layer velocities cannot be compared.

To further evaluate the difference between numerical and experimental data, velocity components along the dashed lines shown in Fig. 5a and b are compared. The y coordinates of locations along the dashed lines correspond to zero, 30%, and 60% of the nozzle geometry y coordinate (y_n) at any horizontal position x. The corresponding velocity profiles are shown in Fig. 6, along with the estimated expanded uncertainty band of the PIV measurements (from $\pm$ 0.2 m/s to $\pm$ 3.8 m/s from the throat to the outlet, respectively). Once again, simulation and experimental data are in good agreement throughout the considered domain, especially in the case of the streamwise component (deviation lower than 1%).

Figure 6b shows that experimental values of v deviate appreciably from simulation values downstream of the nozzle throat, starting from approximately $x = 10mm$. The deviation is up to 9%. This cannot be solely attributed to the error due to the slip velocity for this component, which is calculated in Sec. 2.2 to be less than 2%. Instead, the discrepancy is primarily attributed to the temporal difference between PIV frames, Δt. Due to hardware limitations, Δt could not be reduced below 5μ s, and consequently, particles displacement downstream of the throat ($x > 10mm$) ranges from 1.5 mm to 2 mm. This value is considerably larger than the value of the optimal displacement for the PIV correlation algorithm for the speeds at hand. The consequence thereof is a spatial averaging of the measured velocities along the streamwise direction, mostly evident for the values of the v component, given the substantial variation of velocity gradient along the streamwise direction.

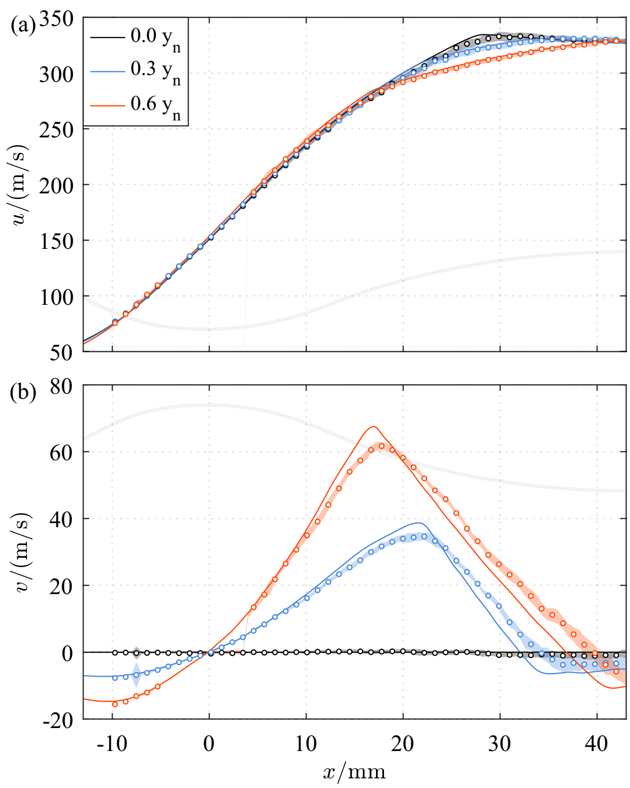

Fig. 6 Streamwise velocity component (**a**) and velocity component normal to the streamwise direction (**b**) at locations featuring y coordinates that are zero, 30%, and 60% of the nozzle cross-section (dashed lines in Fig. 5). Solid lines correspond to values obtained with the RANS simulation, whereas points correspond to values obtained with PIV measurements. Shaded regions indicate the estimated expanded uncertainty range of PIV measurements. The experimental spatial resolution has been reduced by a factor of two for clarity

3.2 Nozzle expansion regions

The flow field within the supersonic nozzle domain can be decomposed into three regions, namely, the kernel, reflex, and uniform regions for analysis purposes Anand et al. (2019). Within the kernel region, flow is accelerated to the desired Mach number, while the reflex region redirects the expanding flow, ensuring a uniform velocity at the nozzle exit.

Identification of these regions from the available numerical and experimental velocity fields can be performed by means of the Q criterion Hunt et al. (1988) and Koláv (2007), Q being a second invariant of $\nabla \boldsymbol{U}$. This criterion is formulated in two dimensions as

$$Q = -\frac{1}{2}\left[\left(\frac{\partial u}{\partial x}\right)^2 + 2\frac{\partial u}{\partial y}\frac{\partial v}{\partial x} + \left(\frac{\partial v}{\partial y}\right)^2\right]. \tag{3}$$

The boundaries of the nozzle expansion regions are characterized by discontinuity of the flow shear, i.e., discontinuities in $Q \leq 0$. Specifically, the boundaries of the uniform region are given by locations for which $Q = 0$.

The estimated Q field obtained from both numerical and experimental data is shown in Fig. 7, including the region boundaries. The figure shows that there is very good agreement between the datasets, albeit the boundary of the uniform region obtained from experimental data is located approximately 4% downstream with respect to the corresponding boundary derived from numerical estimations. This is a direct consequence of the spatial averaging of the velocity fields due to the sub-optimal Δt and, hence, of the velocity gradients along the streamwise direction.

4 Concluding remarks

This work contributes the first application of the PIV measurement technique to the supersonic expansion of an organic vapor flow starting from mildly nonideal thermodynamic states, therefore in the NICFD regime. The result is made possible by the continuous operation capabilities of the ORCHID facility. A very good match between the measured flow velocities and the estimates of a RANS

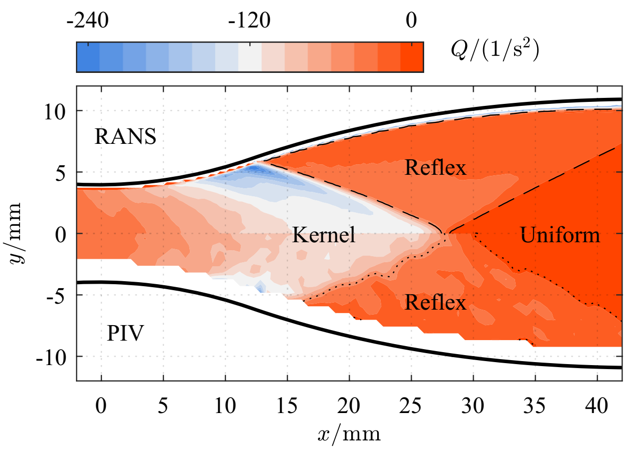

Fig. 7 Kernel, reflex, and uniform regions identified by means of the Q criterion Hunt et al. (1988) and Koláv (2007). The regions obtained from the RANS simulation results are displayed in the upper part of the figure, while those obtained from PIV measurements are shown in the lower part

simulation was observed. The accuracy of the RANS simulation was previously assessed by comparing calculated Mach and pressure fields with Mach number estimations obtained from schlieren images and static pressure measurements along the nozzle profile. These velocity measurements, therefore, prove the reliability and accuracy of the implemented PIV method. Due to the discussed limitations of the current PIV setup, the maximum deviation of the measurements from the simulation data occurs for v velocity component, and it is lower than 10%. Refractive index effects due to the expanding organic vapor were estimated, and it was concluded that for the current experimental conditions, the apparent displacement due to diffraction index variations is smaller than the camera pixel size; hence, expanded uncertainties of the time-averaged velocity field (from $\pm$ 0.2 m/s to $\pm$ 3.8 m/s, 0.06% to 1.1% relative to the maximum velocity) are purely due to the PIV methodology.

Upcoming experiment iterations will focus on improving the PIV method by controllably injecting higher quantities of tracer particles (TiO_2) and by adapting the hardware in order to reduce Δt, thus mitigating the spatial averaging of the velocity field. The characterization of nozzle expansions starting from a fluid at the inlet featuring higher total temperature and pressure is also planned. NICFD effects will, therefore, be more prominent. The appropriate strategy for managing the increased optical distortions due to the refractive index gradients will, therefore, be established. Ultimately, validated numerical (RANS) tools together with the reliable PIV technique are, together, expected to enable investigations for designing and characterizing stators of small-capacity ORC turbines.

Acknowledgements The authors gratefully acknowledge Sietse Kuipers and Eline van den Heuvel for performing the DLS measurements and their help with the interpretation of results

Funding The research work was conducted in the framework of a research program on waste heat recovery systems for more electric aircraft funded by the Applied and Engineering Sciences Division (TTW) of the Dutch Organization for Scientific Research (NWO), Technology Program of the Ministry of Economic Affairs, Grant No. 17906.

Data availability The data supporting the findings of this study can be made available upon reasonable request.

Declarations

Conflict of interest Not applicable. The authors declare no conflict of interest.

Ethical approval Not applicable.

References

Anand N, Vitale S, Pini M, Otero GJ, Pecnik R (2019) Design methodology for suoersonic radial vanes operating in nonideal flow conditions. J Eng Gas Turbines Power 141(2):022601

Baumgärtner D, Otter JJ, Wheeler APS (2020) The effect of isentropic exponent on transonic turbine performance. J Turbomach 142(8):081007

Bills L (2020) Validation of the SU2 flow solver for classical NICFD., Master's thesis (school Delft University of Technology)

Conti C, Fusetti A, Spinelli A, Guardone A (2022) Shock loss measurements in non-ideal supersonic flows of organic vapors. Exp Fluids 63(7):117

Economon TD, Palacios F, Copeland SR, Lukaczyk TW, Alonso JJ (2015) SU2: an open-source suite for multiphysics simulation and design. AIAA J 54(3):828–846

Fuentes-Monjas B, Head AJ, De Servi C, Pini M (2023) Validation of the SU2 fluid dynamic solver for isentropic non-ideal compressible flows. In: White M, Samad TE, Karathanassis I, Sayma A, Pini M, Guardone A (eds) Proceedings of the 4th International Seminar on Non-Ideal Compressible Fluid Dynamics for Propulsion and Power. Springer Nature Switzerland, Cham, pp. 91–99

Gallarini S, Cozzi F, Spinelli A, Guardone A (2021) Direct velocity measurements in high-temperature non-ideal vapor flows. Exp Fluids 62(10):199

Gallarini S, Spinelli A, Cozzi F, Guardone A (2016) Design and commissioning of a laser Doppler velocimetry seeding system for non-ideal fluid flows. In: 12th international conference on heat transfer, fluid mechanics and thermodynamics 2016

Gori G, Zocca M, Cammi G, Spinelli A, Congedo PM, Guardone A (2020) Accuracy assessment of the non-ideal computational fluid dynamics model for siloxane mdm from the open-source su2 suite. Eur J Mech B/Fluids 79:109–120. https://doi.org/10.1016/j.euromechflu.2019.08.014

Guardone A, Colonna P, Pini M, Spinelli A (2024) Nonideal compressible fluid dynamics of dense vapors and supercritical fluids. Annu Rev Fluid Mech 56:1–30. https://doi.org/10.1146/annurev-fluid-120720-033342

Head AJ (2021) Novel experiments for the investigation of non-ideal compressible fluid dynamics: The ORCHID and first results of optical measurements, Ph.D. thesis (school Delft University of Technology)

Head AJ, Novara M, Gallo M, Schrijer F, Colonna P (2019) Feasibility of particle image velocimetry for low-speed unconventional vapor flows. Exp Therm Fluid Sci 102:589–594

Head AJ, Michelis T, Beltrame F, Monjas BF, Casati E, De Servi C (2023) Mach number estimation and pressure profile measurements of expanding dense organic vapors. In: Proceedings of the 4th international seminar on non-ideal compressible fluid dynamics for propulsion and power. NICFD 2022. ERCOFTAC Series, edited by Martin White, Tala El Samad, Ioannis Karathanassis, Abdulnaser Sayma, Matteo Pini, and Alberto Guardone (publisher Springer Nature Switzerland, Cham) pp 229–238

Hunt JCR, Wray AA, Moin P (1988) Eddies, stream and, convergence zones in turbulent flow, Tech. Rep. CTR-S88 (institution Center for Turbulence Research) 193–208

International Standard ISO22412 (2017) Particle size analysis—dynamic light scattering, standard (institution International Organization for Standardization)

Kolář V (2007) Vortex identification: new requirements and limitations. Int J Heat Fluid Flow 28(4):638–652

Lakkad H (2017) NICFD and the PIV technique: feasibility in low speed and high speed flows., Master's thesis (school Delft University of Technology)

Lemmon EW, Bell, IH, Huber, ML, McLinden MO (2018) NIST Standard Reference Database 23: Reference Fluid Thermodynamic and Transport Properties-REFPROP, Version 10.0, National Institute of Standards and Technology

Manfredi M, Persico G, Spinelli A, Gaetani P, Dossena V (2023) Design and commissioning of experiments for supersonic orc nozzles in linear cascade configuration. Appl Therm Eng 224:119996

Pini M, Vitale S, Colonna P, Gori G, Guardone A, Economon T, Alonso JJ, Palacios F (2017) SU2: the open-source software for non-ideal compressible flows. In: Journal of Physics: Conference Series, Vol. 821 (IOP Publishing) p 012013. https://iopscience.iop.org/article/10.1088/1742-6596/821/1/012013/pdf

Ragni D, Schrijer F, van Oudheusde BW, Scarano F (2011) Particle tracer response across shocks measured by PIV. Exp FLuids 50:53–64

Robertson M, Newton P, Chen T, Costall A, Martinez-Botas R (2020) Experimental and numerical study of supersonic non-ideal flows for organic rankine cycle applications. J Eng Gas Turbines Power 142(8):081007

Scarano F (2001) Iterative image deformation methods in PIV. Meas Sci Technol 13(1):R1–R19

Scarano F, van Oudheusden BW (2003) Planar velocity measurements of a two-dimensional compressible wake. Exp Fluids 34:430–441

Scarano F, Riethmuller M (2000) Advances in iterative multigrid PIV image processing. Exp Fluids 29:S051–S060. https://doi.org/10.1007/s003480070007

Schiacchitano A, Wieneke B (2016) PIV uncertainty propagation. Meas Sci Technol 27(8)

Spinelli A, Cammi G, Gallarini S, Zocca M, Cozzi F, Gaetani P, Dossena V, Guardone A (2018) Experimental evidence of non-ideal compressible effects in expanding flow of a high molecular complexity vapor. Exp Fluids 59:1–16

Spinelli A, Guardone A, De Servi C, Colonna P, Reinker F, Stefan aus der W, Miles R, Martinez-Botas RF (2020) Experimental facilities for non-ideal compressible vapour flows. ERCOFTAC BULLETIN 124:59–66

Stetefeld J, McKenna SA, Trushar RP (2016) Dynamic light scattering: a practical guide and applications in biomedical sciences. Biophys Rev 8:409–427

Stöhr M, Boxx I, Carter CD, Meier W (2012) Experimental study of vortex-flame interaction in a gas turbine model combustor. Combust Flame 159:2636–2649

Ueno S, Tsuru W, Kinoue Y, Shiomi N, Setoguchi T (2015) PIV measurement of carbon dioxide gas-liquid two-phase nozzle flow. In: ASME proceedings: symposium on noninvasive measurements in single and multiphase flows, fluids engineering division summer meeting, Vol. Volume 1A: Symposia, Part 2, p V01AT20A002

Urban WD, Mungal MG (2001) Planar velocity measurements in compressible mixing layers. J Fluid Mech 431:189–222

van der Stelt TP, Nannan NR, Colonna P (2012) The iPRSV equation of state. Fluid Phase Equilibria 330:24–35

Valori V, Elsinga GE, Rohde M, Westerweel J, van Der Hagen THJJ (2019) Particle image velocimetry measurements of a thermally convective supercritical fluid. Exp Fluids 60:1–14

Vitale S, Albring TA, Pini M, Gauger NR, Colonna P (2017) Fully turbulent discrete adjoint solver for non-ideal compressible flow applications. J Glob Power Propuls Soc 1:252–270

Vitale S, Gori G, Pini M, Guardone A, Economon TD, Palacios F, Alonso JJ, Colonna P (2015) Extension of the su2 open source cfd code to the simulation of turbulent flows of fuids modelled with complex thermophysical laws. In: 22nd AIAA computational fluid dynamics conference, p 2760

Westerweel J, Scarano F (2005) Universal outlier detection for PIV data. Exp Fluids 39:1096–1100

Zocca M, Guardone A, Cammi G, Cozzi F, Spinelli A (2019) Experimental observation of oblique shock waves in steady non-ideal flows. Exp Fluids 60:1–12